SCIENTIFIC REPORTS

OPEN

Study of the lithium diffusion properties and high rate performance of $TiNb_6O_{17}$ as an anode in lithium secondary battery

Received: 4 August 2017
Accepted: 13 November 2017
Published online: 30 November 2017

Yong-Seok Lee & Kwang-Sun Ryu

$TiNb_6O_{17}$ and $TiNb_2O_7$ were synthesized using a solid-state method. The techniques were used to assess the electrochemical performance and lithium diffusion kinetics of $TiNb_6O_{17}$ related to the unit cell volume with $TiNb_2O_7$. The charge-discharge curves and cyclic voltammetry revealed $TiNb_6O_{17}$ to have a similar redox potential to $TiNb_2O_7$ as well as a high discharge capacity. The rate performance of $TiNb_6O_{17}$ was measured using a rate capability test. SSCV and EIS showed that $TiNb_6O_{17}$ had higher lithium diffusion coefficients during the charging. From GITT, the lithium diffusion coefficients at the phase transition region showed the largest increase from $TiNb_2O_7$ to $TiNb_6O_{17}$.

Lithium secondary batteries have been studied for large scale energy devices, such as electric vehicles (EVs) and energy storage systems (ESSs), requiring high energy density and superior rate performance. The development of anode materials has been investigated due to importance of the charge rate and good reversibility for lithium secondary batteries. Commercial anode materials for batteries, such as graphite, have high capacities (370mAh/g). On the other hand, the active material has some problems, such as irreversible capacity loss, due to solid electrolyte interface (SEI) layer and lithium dendrite formation due to the low working voltage window at 0.8 V[1]. In particular, lithium dendrite formation leads to the safety hazard of lithium secondary batteries and the unsuitability of the active materials for batteries[1–3]. The Si based materials such as SiO_2 showed also high capacity but could not be used to high volume expansion[4]. In contrast, titanium-based anode materials allow lithium batteries to avoid SEI and lithium dendrite formation due to their safe working voltage area using the Ti^{4+}/Ti^{3+} redox reaction (~1.5 V vs. Li/Li^+)[2]. Typically, $Li_4Ti_5O_{12}$ has been studied because of its working voltage area and zero strain properties, resulting in good rate performance due to its strong Ti-O covalent bond[3]. Despite this, the material has a low theoretical capacity (175mAh/g) and is unsuitable for large-scale devices.

Recently, titanium niobium oxide (TNO) materials, such as $TiNb_2O_7$ and $Ti_2Nb_{10}O_{29}$, have been introduced as promising titanium-based anode materials owing to their nontoxic, good rate performance, low volume change, stable working voltage window (1–2.5 V), and high theoretical capacity (387~390mAh/g). The capacities of TNO materials are influenced by many redox reactions, such as one Ti (Ti^{3+}/Ti^{4+}) and two Nb reactions (Nb^{3+}/Nb^{4+} and Nb^{4+}/Nb^{5+})[5,6]. On the other hand, they have lower capacity and reversibility than their theoretical capacities due to the low electric conductivity and lithium diffusion properties into the structure called Wesley-Roth 2D structure[7–9]. To solve these problems, many studies have been conducted to achieve TNO materials with high reversible capacity and improved rate performance, such as doping with other metals (Ru, Mo, etc.) to achieve high ionic conductivity and electrical conductivity and controlling the particle shape and size[1–3,6–12]. Chunfu Lin *et al.* examined $TiNb_6O_{17}$, which is a new TNO material. The material is composed a large number of Nb ions and has a higher theoretical capacity (397 mA/g) than $TiNb_2O_7$ and $Ti_2Nb_{10}O_{29}$. Moreover, the material has the same Wisely-Roth structure (monoclinic) but larger lattice parameters and unit cell volume than $TiNb_2O_7$ and $Ti_2Nb_{10}O_{29}$ (1122.541 Å vs. 803.21 Å, 1118.512 Å) due to the larger number of Nb^{5+} ions with a larger size (0.64 Å) than that of Ti^{4+} ions (0.605 Å)[13–15]. This causes a more open lithium insertion/insertion site and improved rate performance; the schema of this theory is listed in Fig. 1. The material showed a higher discharge capacity and better lithium diffusion coefficients by charge-discharge, rate capability, and slow scan cyclic voltammetry (SSCV) than $Ti_2Nb_{10}O_{29}$ in Chunfu's study[13].

Department of Chemistry, University of Ulsan, Ulsan, 680-749, Korea. Correspondence and requests for materials should be addressed to K.-S.R. (email: ryuks@ulsan.ac.kr)

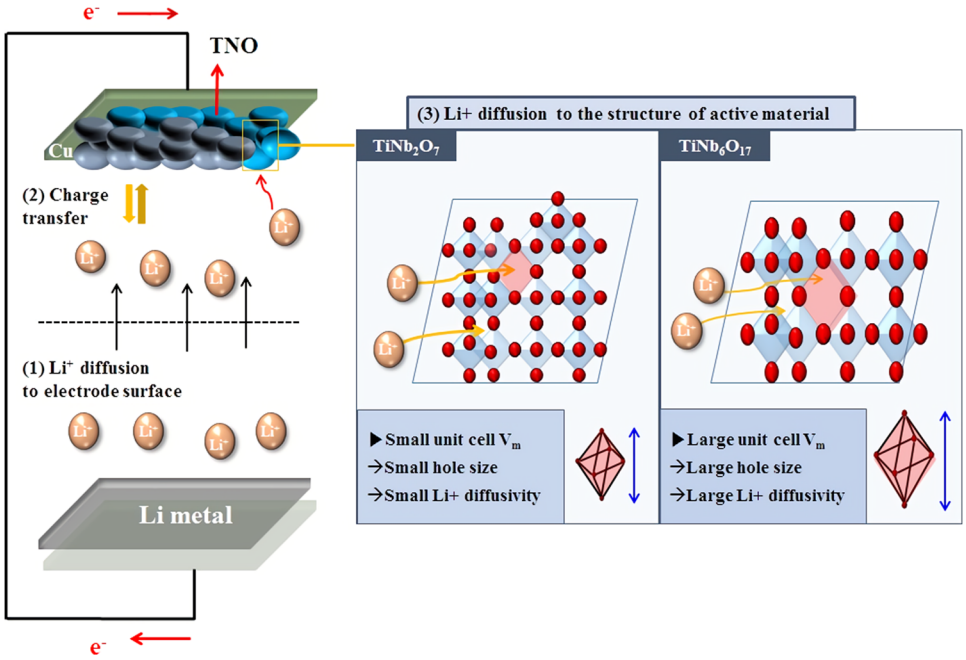

Figure 1. Schematic diagram of the kinetic mechanism of lithium diffusion in Li secondary batteries and phenomena about the unit cell size.

Therefore, this study examined the accurate lithium diffusion kinetics and electrochemical performance of $TiNb_6O_{17}$ compared to $TiNb_2O_7$ which has the smallest unit cell volume among the TNO materials and can clearly be compared with $TiNb_6O_{17}$. The materials were synthesized using a solid-state method. For electrochemical analysis, the charge-discharge curves and rate capability tests were conducted to determine their electrochemical performance. To examine the lithium diffusion kinetics, SSCV, electrochemical impedance spectroscopy (EIS), and a galvanostatic intermittent titration technique (GITT) were used. As a result, $TiNb_6O_{17}$ showed higher discharge capacity (284mAh/g vs. 264mAh/g) and better rate performance than $TiNb_2O_7$ (82mAh/g vs. 20mAh/g at 30 C). In addition, $TiNb_6O_{17}$ showed higher lithium diffusion coefficients than $TiNb_2O_7$ (mean value 10^{-12} S^2/m vs. 10^{-13} S^2/m).

Experimental

Synthesis of the active materials and characterization. $TiNb_2O_7$ and $TiNb_6O_{17}$ were synthesized by a solid-state reaction method using TiO_2 (99.9%, Rare Metallic) and Nb_2O_5 (99.99%, Sigma-Aldrich) powders as the starting materials. TiO_2 and Nb_2O_5 were mixed by ball milling at a stoichiometric molar ratio for 4 h at 300 rpm. The mixed powder was pressed into pellets and calcined in air 1300 °C for 12 h (5 °C/min). The morphology and Ti and Nb content in the two TNO materials were observed by field-emission scanning electron microscopy (FE-SEM, Jeol JSM6500F) and energy dispersion spectroscopy (EDS) attached to FE-SEM. The crystalline structures of the materials were analyzed by X-ray powder diffraction (XRD, Rigaku, Ultima4) was conducted using Ka1 radiation at 45KV/40 mA in the range, 10–100° (2θ). Fourier-transform infrared spectroscopy (FT-IR, Shimadzu IR AFFInity-1S) and X-ray photoelectron spectroscopy (XPS, ThermoFisher K-alpha) were used to examine the chemical bonding and oxidation state of the TNO materials, respectively.

Coin cell assembly and electrochemical analysis. The composition of the TNO anodes was a mixture of active material ($TiNb_2O_7$ or $TiNb_6O_{17}$, 70 wt. %), conducting agent (Super-P, 20 wt. %), and polyvinylidene fluoride binder (PVdF 5130, 10 wt. %). The materials were mixed by ball-milling in 1-methyl-2-pyrrolidinone (NMP) until a viscous slurry formed and cast on Cu foil. The electrochemical properties were tested in CR2032-type coin cells. The cells were assembled with a TNO electrode as the working electrode and lithium metal as the counter electrode separated by a membrane with polypropylene in an Ar-filled glove box. The electrolyte was 1 M $LiPF_6$ dissolved in a mixture of ethylene carbonate (EC) and dimethyl carbonate (DMC) with a volume ratio 1:2. Cyclic voltammetry (CV) was conducted using a battery cycler (Won A tech, WBCS3000) at a scan rate of 0.1mVs^{-1} and ranging from 0.05–0.3 mVs^{-1} from 3.0 to 1.0 V (versus Li/Li^+). Galvanostatic charge-discharge tests were performed using the battery cycles at 0.1 C (38.7mAg^{-1} of $TiNb_2O_7$ and 39.7mAg^{-1} of $TiNb_6O_{17}$) from 3.0 to 1.0 V. The rate capabilities were conducted over the voltage range of 3.0–1.0 V with a current density range 1.0 C to 30 C at room temperature. EIS was carried out by applying an AC signal of 5 mV amplitude over the frequency range from 100KHz to 10mHz using an electrochemical analyzer (NeoSience, SP-300). GITT was tested at a current density of 0.1 C over the voltage range of 3.0–1.0 V using the electrochemical analyzer. The procedure of GITT consisted of galvanostatic charge pulses for each duration time (15 min), followed by a relaxation time (30 min).

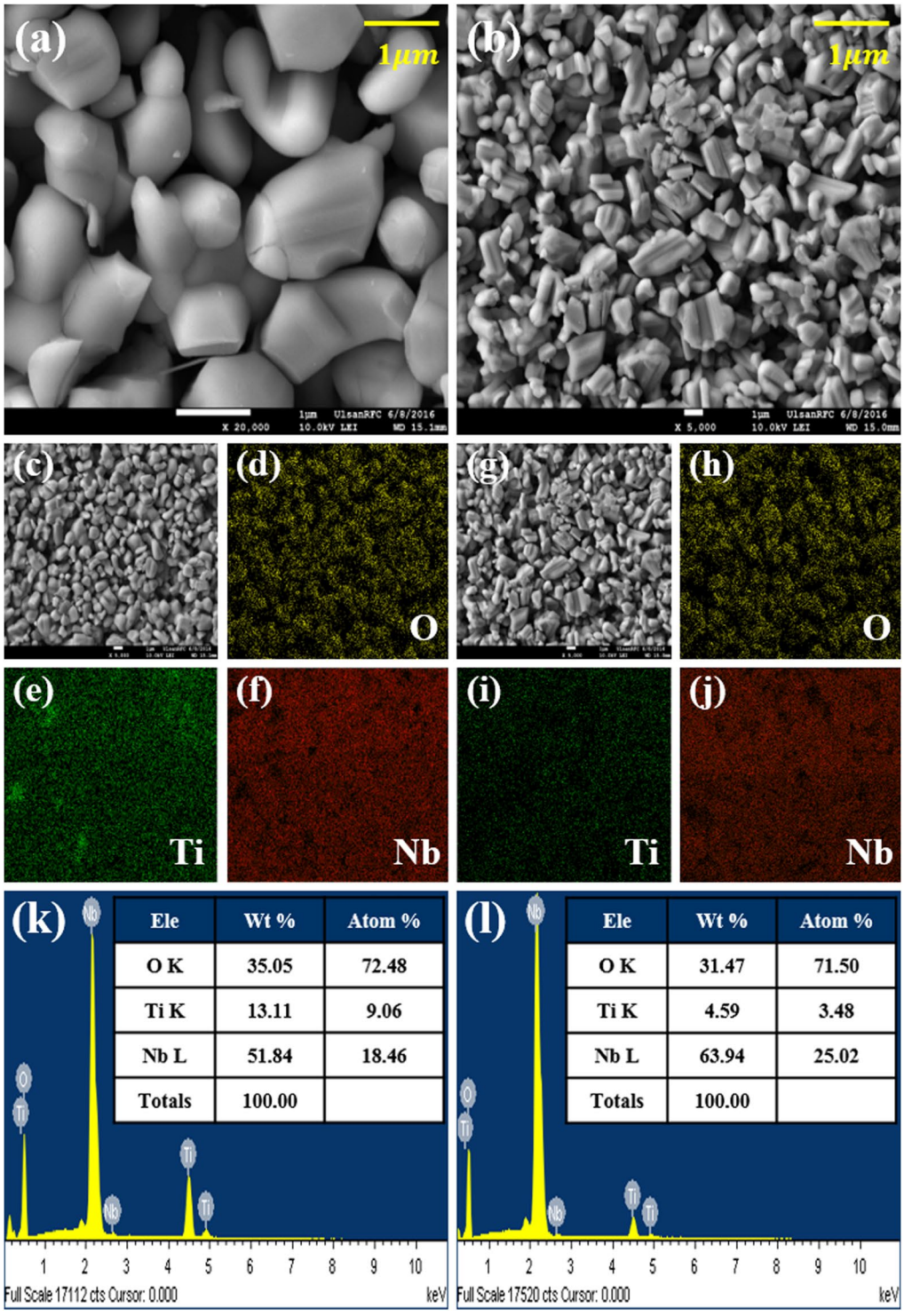

Figure 2. (**a**) SEM images of $TiNb_2O_7$ and (**b**) $TiNb_6O_{17}$ (magnification ×20,000), (**c**) SEM images of $TiNb_2O_7$ (magnification ×5,000), (**d**)~(**f**) EDS mapping images of oxygen (yellow), titanium (green), and niobium (red), (**g**) SEM images of $TiNb_6O_{17}$ (magnification ×5,000), and (**h**)~(**i**) EDS mapping images of oxygen, titanium, and niobium, and (**k**) the results of EDS analysis of $TiNb_2O_7$ and (l) $TiNb_6O17$.

Results and Discussion

Characterization. Figure 2(a),(b) shows SEM images (magnification ×20,000) of $TiNb_2O_7$ and $TiNb_6O_{17}$. A comparison of the particle size and morphology was not accurate due to irregular particle formation by solid state synthesis. On the other hand, the morphologies of the two materials were similar in principle. The mean particle size of the two samples was approximately 1–3 μm. Figure 2(c)~(f) and (g)~(j) present SEM images of (c) $TiNb_2O_7$ and (g) $TiNb_6O_{17}$ (magnification ×5,000) and EDS mapping images of (d) oxygen, (e) titanium, and

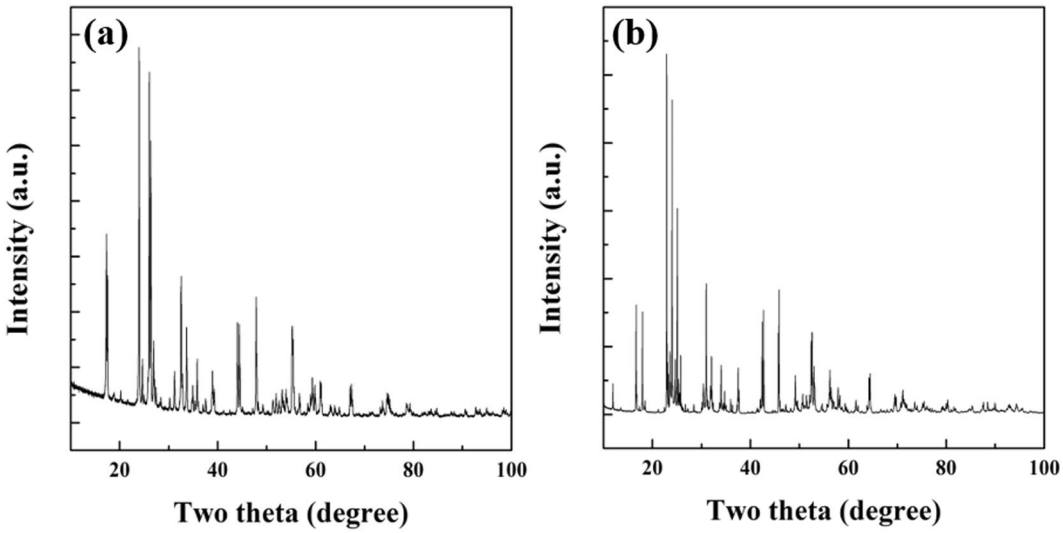

Figure 3. XRD patterns of (**a**) $TiNb_2O_7$ and (**b**) $TiNb_6O_{17}$.

(f) niobium in $TiNb_2O_7$ and (h) oxygen, (i) titanium, and (j) niobium in TiN_6O_{17}. The calculated atomic percentages of the two materials by EDS are presented in Fig. 2(k) $TiNb_2O_7$ and (l) $TiNb_6O_{17}$. The mapping images of Ti and Nb of the two materials exhibited similar dispersion. On the other hand, the images of Ti in $TiNb_2O_7$ and $TiNb_6O_{17}$ showed different dispersion and brightness. Ti in $TiNb_6O_{17}$ was darker than that of $TiNb_2O_7$. The brightness means that the Ti content in $TiNb_6O_{17}$ is lower than that of $TiNb_2O_7$. These results correspond to atomic percentages of Ti and Nb in the two materials. The atomic percentage ratio of Nb and Ti in $TiNb_2O_7$ was 1:2 (Ti:Nb = 9.06:18.46), whereas the Nb: Ti ratio in $TiNb_6O_{17}$ was approximately 1:7 (Ti:Nb = 3.48:25.02). These results show that the molar ratio of Nb and Ti is different in the two TNO materials.

Figure 3 (a) $TiNb_2O_7$ and (b) $TiNb_6O_{17}$ present XRD patterns of the two TNO materials. The pattern of $TiNb_2O_7$ was well indexed to the calculated patterns according to the monoclinic symmetry of $TiNb_2O_7$ with the monoclinic ReO_3 shear structure with the space group C2/m (JCPDS card No. 70–2009);[6] however, there have been no studies of $TiNb_6O_{17}$. Therefore, there is no calculated structural data for $TiNb_6O_{17}$. On the other hand, the XRD patterns of $Ti_2Nb_{10}O_{29}$ have been reported in many studies, which is similar to that of $TiNb_6O_{17}$[13]. Therefore, $TiNb_6O_{17}$ has a similar crystal structure to $Ti_2Nb_2O_{29}$, which is a Wadsley-Roth shear structure with an A2/m space group. Compared to the XRD patterns of calculated $Ti_2Nb_{10}O_{29}$ and $TiNb_6O_{17}$ synthesized in this study, most peak positions and intensities were in good agreement except for two main peak intensities, which coincides with the XRD patterns reported by Chunfu Lin. The powder XRD patterns of TiNb6O17 was refined with the fullprof software and the rietveld parameters are a = 15.48089 Å, b = 3.81501 Å, c = 20.62921 Å, α&γ = 90°, β = 113.106°, and V = 1218.356 Å^3. The calculated rietveld refinement parameters of $TiNb_6O_{17}$ is well matched the with the crystalline parameters of $Ti_2Nb_{10}O_{29}$[13].

FT-IR spectroscopy was conducted to characterize the Ti-O and Nb-O bond of $TiNb_2O_7$ and $TiNb_6O_{17}$. Figure 4(a) presents the FT-IR spectra of two samples. The peaks at 924 cm^{-1} and 520 cm^{-1} correspond to the stretching vibrations of the Nb-O bonds and Nb-O-Nb bridging bonds and the stretching vibration of at 694 cm^{-1} and 839 cm^{-1} are Ti-O-Ti bonds[12]. The BET specific surface area and volume of the TNO materials were studied by nitrogen adsorption techniques; Fig. 4(b) shows the corresponding isotherm. The specific surface area of $TiNb_2O_7$ and $TiNb_6O_{17}$ is 2.66 m^2/g and 2.36 m2/g; the mean pore volume of the materials is 0.11 cm^3/g and 0.10 cm^3/g respectively. As the measurement was conducted by using standard multi point BET, the specific surface area of two materials is almost same. The results are corresponded to the SEM images showing similar particle size of two materials. Therefore, the surface area of the electrodes made by two TNO materials is also same and have not an effect on the electrochemical analysis such as lithium diffusion analysis.

XPS was used to analyze the chemical oxidation state of Ti and Nb in the samples, as shown in Fig. 5. Figure 5(a) $TiNb_2O_7$ and (c) $TiNb_6O_{17}$ showed Ti $2p_{1/2}$ and $2p_{3/2}$ peaks at 464.18 eV & 458.38 eV ($TiNb_2O_7$), and 464.18 eV & 458.18 eV ($TiNb_6O_{17}$), respectively. These binding energies were similar and corresponded to the binding energies of Ti^{4+} in TiO_2[3,5,6,8]. The noise of the Ti spectra was attributed to the smaller content than Nb. In particular, the spectra of Ti in $TiNb_6O_{17}$ showed more noise than that of $TiNb_6O_{17}$. This may be because $TiNb_6O_{17}$ is composed of a lower Ti content than $TiNb_2O_7$. These results match the results of EDS analysis and the mapping images. Figure 5(b) $TiNb_2O_7$ and (d) $TiNb_6O_{17}$ present the spectra of Nb^{5+} in Nb_2O_5.The Nb $3d_{3/2}$ and Nb $3d_{5/2}$ peaks were located at (b) 209.88 & 207.18 and (c) 209.68 & 206.98. These values agree with the binding energies of Nb^{5+} in Nb_2O_5[3,5,10]. Therefore, FT-IR spectroscopy and XPS shows that the two TNO materials are composed with Ti^{4+} in TiO_2 and Nb^{5+} in Nb_2O_5.

Electrochemical analysis. Figure 6 (a),(b) presents the charge and discharge curves of $TiNb_2O_7$ and $TiNb_6O_{17}$ at a current density of 0.1 C (38.7 mAg^{-1} and 39.7 mAg^{-1}) over the voltage range of 3.0–1.0 V. The curves of the two TNO anodes showed three plateau regions. The regions 1 and 3 are the solid-solution region[6,9]. These regions mean the redox reaction of $Ti^{4+} \leftrightarrow Ti^{5+}$ and $Nb^{3+} \leftrightarrow Nb^{4+}$, respectively. Region 2 is a two-phase

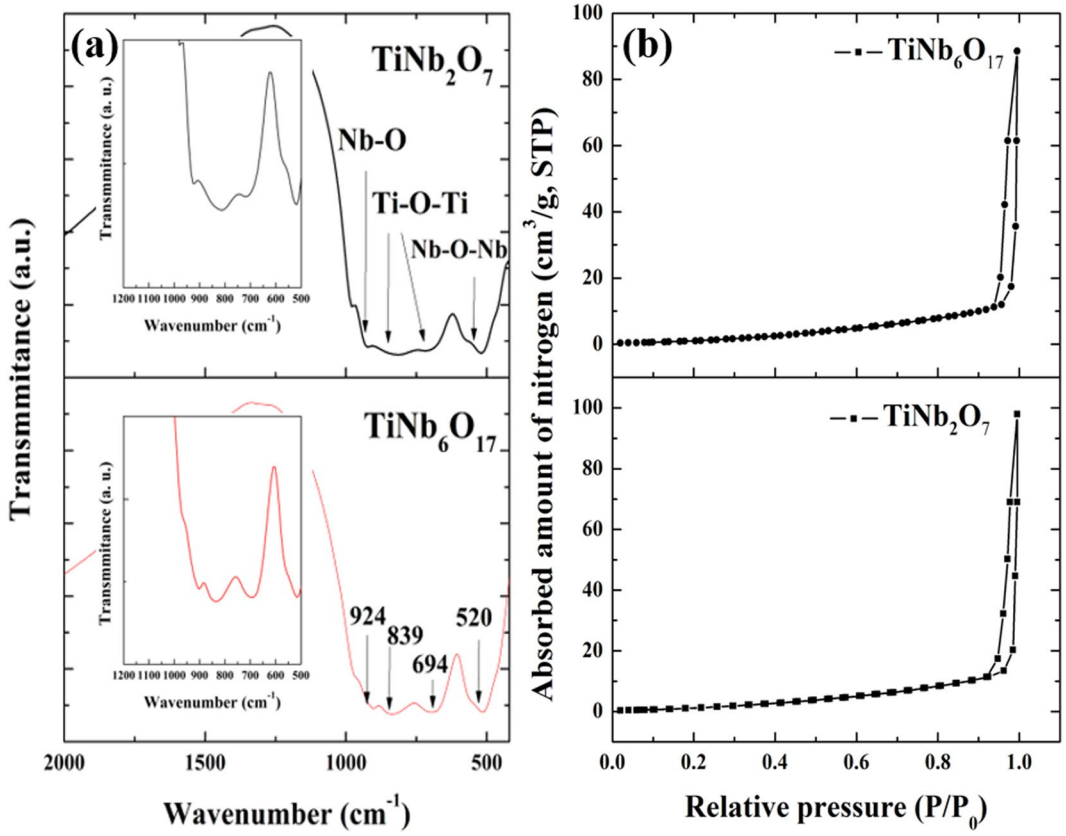

Figure 4. FT-IR spectra in Fig. (**a**) and nitrogen adsorption-desorption isotherm in Fig. (**b**) of two TNO materials.

reaction, which means the reaction of $Nb^{4+} \leftrightarrow Nb^{5+}$[3,5–13]. Compared to the initial discharge capacities, $TiNb_6O_{17}$ exhibited a larger discharge capacity (284 $mAhg^{-1}$) than that of $TiNb_2O_7$ (264 $mAhg^{-1}$). In addition, the irreversibility of $TiNb_6O_{17}$ was smaller than $TiNb_2O_7$ particularly from the 1st to 2nd cycles. CV of $TiNb_2O_7$ and $TiNb_6O_{17}$ was conducted at a scan rate of 0.1mVs^{-1} from 3.0 V to 1.0 V and from 3.0 and 1.0 V for 10 cycles. As shown in Fig. 6(c) $TiNb_2O_7$ and (d) $TiNb_6O_{17}$, both curves Fig. 6(a) $TiNb_2O_7$ and curve (b) $TiNb_6O_{17}$ showed three current peaks at the oxidation and reduction state, respectively. Each peak is expressed in the curves (C_p and A_p mean the cathodic peaks and anodic peaks). Although the reduction peaks were C_{p1} ($Ti^{4+} \rightarrow Ti^{3+}$), C_{p2} ($Nb^{5+} \rightarrow Nb^{4+}$), and C_{p3} ($Nb^{4+} \rightarrow Nb^{3+}$), A_{p1}, A_{p2}, and A_{p3} mean the oxidation reaction of $Nb^{3+} \rightarrow Nb^{4+}$, $Nb^{4+} \rightarrow Nb^{5+}$, and $Ti^{3+} \rightarrow Ti^{4+}$[10,15]. These potential regions of the current peaks were matched with the plateau regions in charge and discharge curves. These results show that the reaction mechanisms of the two TNO materials are the same. In addition, the reaction of $Nb^{4+} \leftrightarrow Nb^{5+}$, which is corresponded to two-phase regions in the charge and discharge curves, showed the highest current peak area and is regarded as the main reaction. Compared to the CV curves of $TiNb_2O_7$ and $TiNb_6O_{17}$, $TiNb_6O_{17}$ exhibits higher reactivity and reversibility from the peak area at all cycles. In addition, the decrease in the peak intensity during the cycle, particularly A_{p2} and C_{p1}, suggests that the reversibility of $TiNb_6O_{17}$ is better than $TiNb_2O_7$. This is in agreement with the results of the charge and discharge tests.

To understand the electrochemical performance of the lithium diffusion properties of $TiNb_2O_7$ and $TiNb_6O_{17}$, the rate capabilities were performed at various C-rates from 1 C to 30 C (discharge rate was fixed at 1 C). Figure 7 presents the rate performance of the two TNO materials. A comparison with the average capacities for the 5thcycle at each C-rate revealed $TiNb_6O_{17}$ to have charge capacities of 252, 230, 206, 187, 107, and 80 $mAhg^{-1}$ at 1 C, 2 C, 5 C, 10 C, 20 C, and 30 C, respectively. These values are larger than that of $TiNb_2O_7$ (234, 210, 174, 152, 52, and 19 $mAhg^{-1}$). In particular, the difference in the charge capacities at a high rate (20 C and 30 C) was distinct. When calculating the ratio of the average charge capacity, 30 C/1 C, the ratio was 8.12% for $TiNb_2O_7$ and 31.7% for $TiNb_6O_{17}$, which suggests that $TiNb_6O_{17}$ has better rate properties than $TiNb_2O_7$[13]. In addition, a comparison of the cycling retention at 5 C to 30 C revealed $TiNb_6O_{17}$ to have better cycling properties, whereas $TiNb_2O_7$ exhibited a rapid decrease in capacity. This means the better electrochemical reversibility of the $TiNb_6O_{17}$. These studies including the results of the charge and discharge tests and CV indicated that lithium ion transport of $TiNb_6O_{17}$ is faster than the rate of $TiNb_2O_7$ due to the larger theoretical capacity and better lithium diffusion kinetics by larger lithium site.

Figure 8 presents the CV data of (a) $TiNb_2O_7$ and (b) $TiNb_6O_{17}$ at various scan rates in the range, 0.05–0.3 mVs^{-1}. CV at various scan rates is usually used to study the oxidation and reduction properties in electrochemical reactions and obtain the apparent chemical diffusion coefficient of Li-ions[16–20]. With increasing scan rate, the anodic peaks move to a low potential and the cathodic peaks move to a high potential due to the increasing

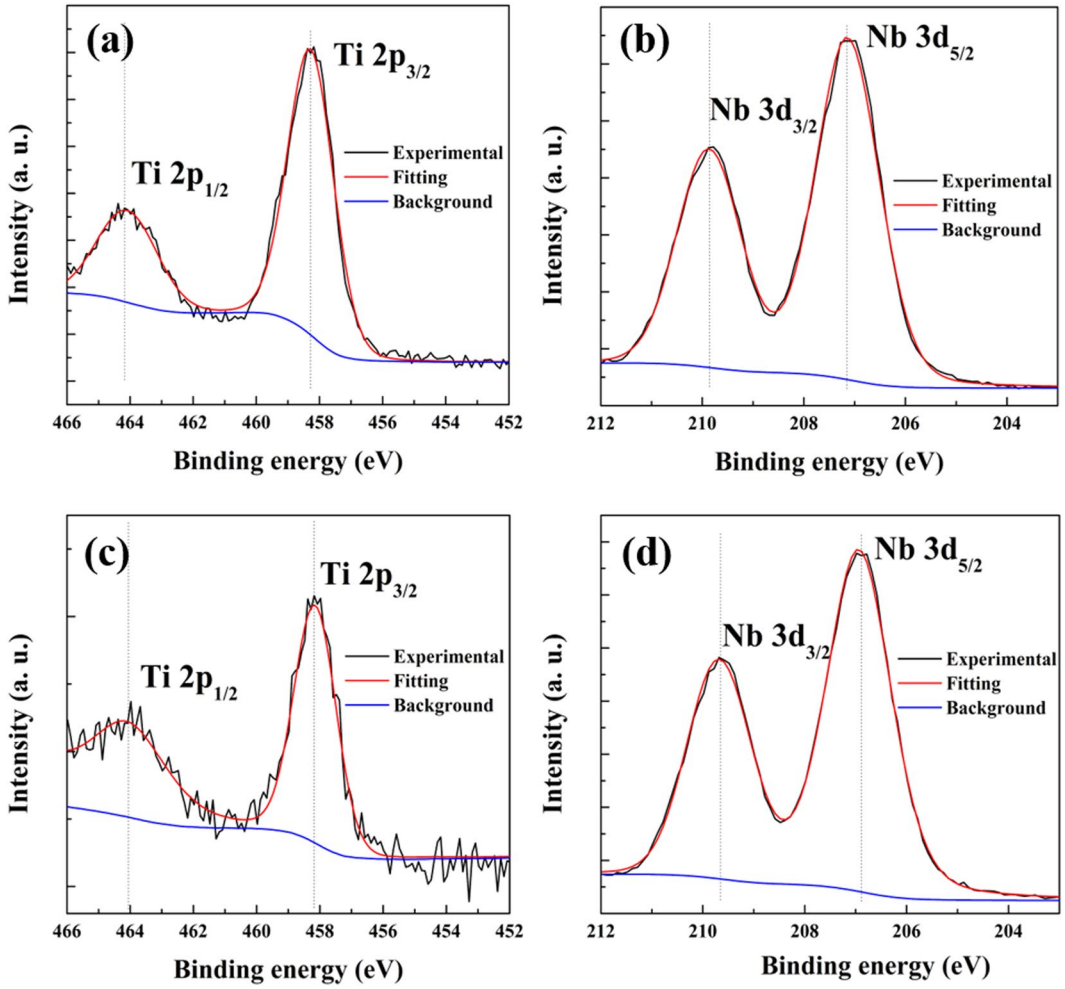

Figure 5. XPS spectra of (**a**) Ti and (**b**) Nb element in $TiNb_2O_7$, (**c**) Ti and (**d**) Nb element in $TiNb_6O_{17}$.

polarization. In addition, the peak intensities of anodic and cathodic reaction increase with increasing scan rate. The peak current density (I_p) revealed a linear relationship with the square root of the scan rate ($v^{-0.5}$), which is expected for a diffusion-controlled process in Fig. 8(c) $TiNb_2O_7$ and (d) $TiNb_6O_{17}$[20–22]. Each color means the linearity of three anodic and cathodic peaks (Black: A_{p1} and C_{p1}, Pink: A_{p2} and C_{p2}, and Purple: A_{p3} and C_{p3}). The relationship and chemical diffusion coefficient can be determined from the Randles-Sevcik equation (Eq. 1)[16,17,23]:

$$Ip = 0.4463n^{3/2}F^{3/2}C_{Li} + SR^{-1}T^{-1}D_{(Li^+)}{}^{1/2}v^{1/2} \quad (1)$$

where n is the charge transfer number; F is Faraday's constant; $C_{Li}{}^+$ is the Li-ion concentration in $TiNb_2O_7$ and $TiNb_6O_{17}$; S is the surface area per weight of active materials; R is the gas constant; and T is the absolute temperature (K). $D_{Li}{}^+$ is the Li-ion diffusion coefficient, and v is the scan rate. In this study, $D_{Li}{}^+$ around three anodic and three cathodic peaks in Fig. 6(c) and (d) was calculated using the above equation. Table 1 lists the calculated $D_{Li}{}^+$. As the results, $TiNb_2O_7$ showed the $D_{Li}{}^+$ value 10^{-14} cm^2/s which is similar to the diffusion coefficient in the previous study (for phase transition region)[24]. Compared to $D_{Li}{}^+$ at the anodic peaks, $D_{Li}{}^+$ of $TiNb_6O_{17}$ was 20 times (A_{p1}), 12 times (A_{p2}), and 38 times (A_{p3}) higher than that of $TiNb_2O_7$. $D_{Li}{}^+$ of the peaks A_{p1} ($Nb^{4+} \rightarrow Nb^{5+}$) and A_{p3} ($Ti^{3+} \rightarrow Ti^{4+}$) of $TiNb_6O_{17}$ was particularly high. Although the gap of $D_{Li}{}^+$ at the A_{p2} ($Nb^{4+} \rightarrow Nb^{5+}$) between $TiNb_2O_7$ and $TiNb_6O_{17}$ was smaller than those of A_{p1} and A_{p3}, the difference was apparent. In the case of $D_{Li}{}^+$ at cathodic peaks, the values of $TiNb_6O_{17}$ were 5 times (C_{p1}, $Nb^{4+} \rightarrow Nb^{3+}$), 15 times ($C_{p2}$, $Nb^{5+} \rightarrow Nb^{4+}$), and 14 times ($C_{p3}$, $Ti^{4+} \rightarrow Ti^{3+}$) higher than those of $TiNb_2O_7$. A comparison of the gap of D between $TiNb_6O_{17}$ and $TiNb_2O_7$ at the anodic peaks revealed the difference in the $D_{Li}{}^+$ values at the cathodic peaks to be low except for C_{p2}. On the other hand, the $D_{Li}{}^+$ of $TiNb_6O_{17}$ at A_{p2} and C_{p2} meaning two phase transition in TNO materials were clearly higher than that of $TiNb_2O_7$(12 and 15 times). In addition, the anodic and cathodic reaction of the TNO anodes means the de-lithiation and lithiation process during oxidation and reduction, respectively. Therefore, the lithium diffusion properties of $TiNb_6O_{17}$ were better than those of $TiNb_2O_7$. The reason is that $TiNb_6O_{17}$ has a larger unit cell volume and more open Li-ion sites than $TiNb_2O_7$. The advanced crystal structure of $TiNb_6O_{17}$ leads to a larger size and number of Li-ion transport paths in the crystal structure, facilitating Li-ion transport during the de-lithiation and lithiation processes[10,12,18].

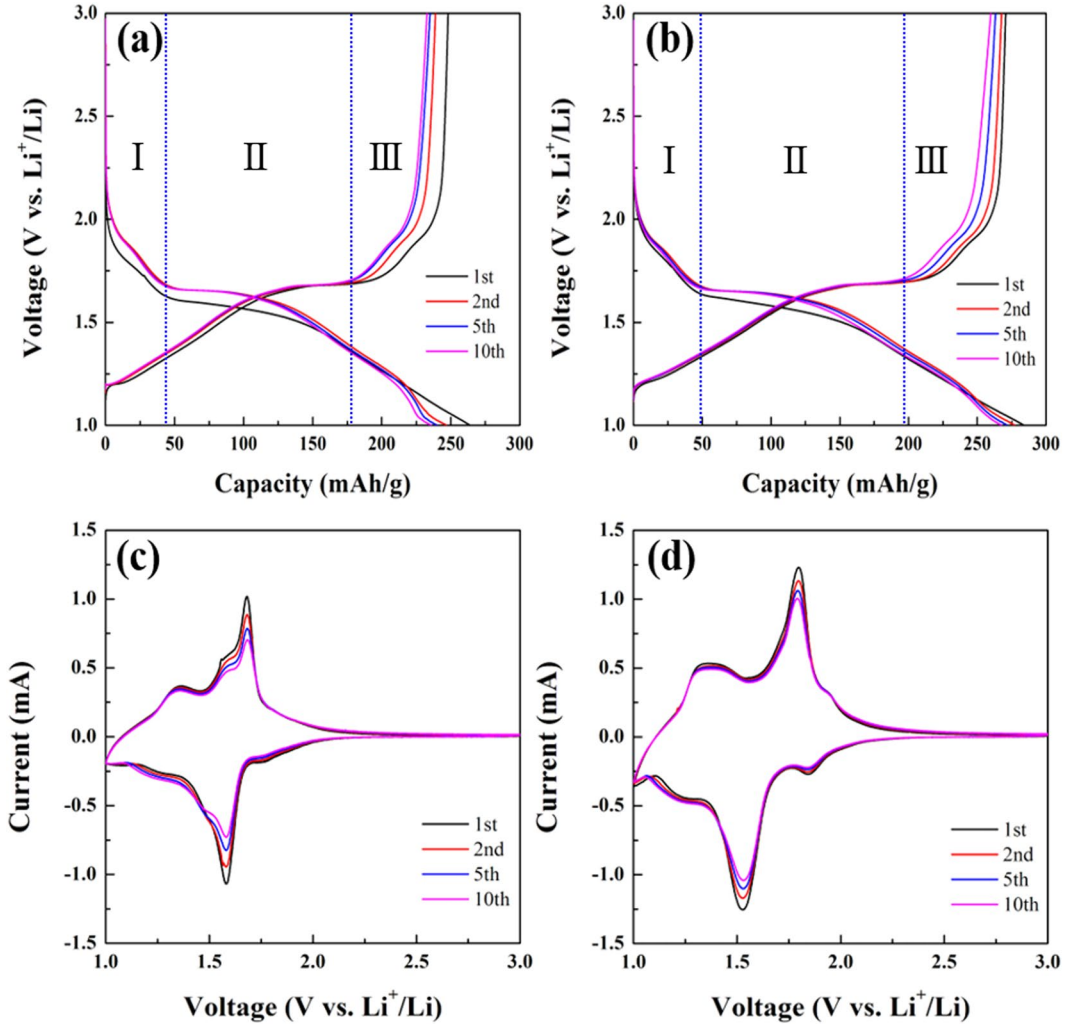

Figure 6. (**a**) Charge/discharge curves of $TiNb_2O_7$ and (**b**) $TiNb_6O_{17}$anodes at 0.1 C, (**c**) cyclic voltammetry of $TiNb_2O_7$ and (**d**) $TTiNb_6O_{17}$anodes in the potential window of 1.0–3.0 V at scan rate of 0.1 mVs^{-1}.

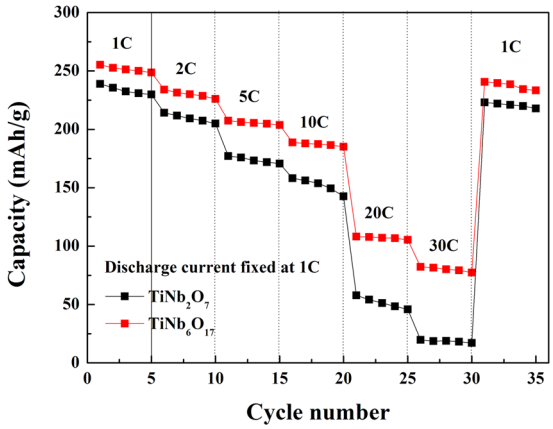

Figure 7. Capacity retention of $TiNb_2O_7$ and $TiNb_6O_{17}$ anodes at various scan rates (1 C, 2 C, 5 C, 10 C, 20 C, and 30 C); the discharge rate was fixed at 1 C.

Figure 9 presents the Nyquist plots of $TiNb_2O_7$ and $TiNb_6O_{17}$ by EIS. EIS has been used to examine electrode materials because it can reveal the relationship between the crystal lattice with the electrochemical properties[24–29]. This technique provides kinetic information that can be related to a specific state-of-charge or discharge (SOC,

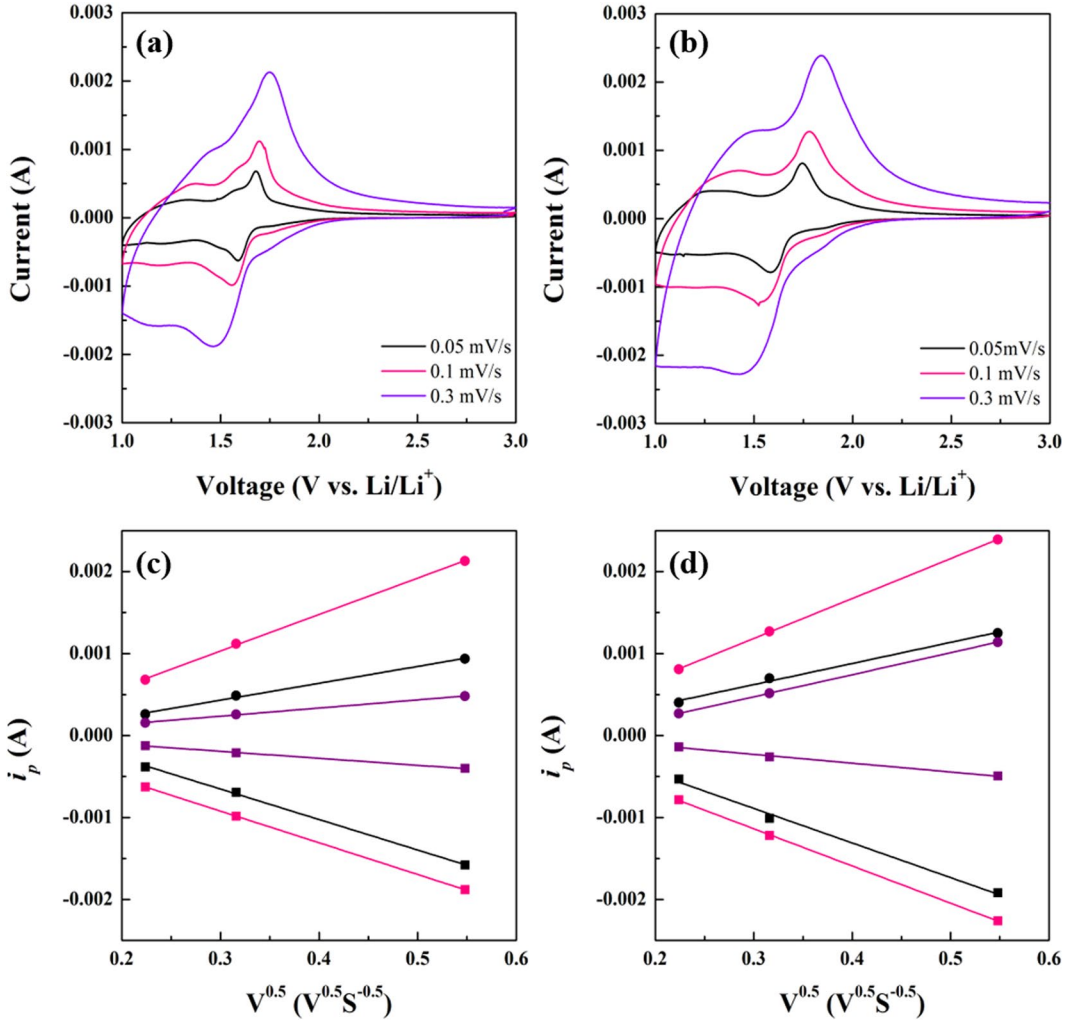

Figure 8. Cyclic voltammetry with various scan rate of (**a**) $TiNb_2O_7$ and (**b**) $TiNb_6O_{17}$, linear relationship between the peak current of the cathodic/anodic reaction and the square root of the sweep rate (**c**) $TiNb_2O_7$ and (**d**) $TiNb_6O_{17}$ (●: anodic, ■: cathodic and linear: linear fitting).

$TiNb_2O_7$	Anodic peak			Cathodic peak		
D_{Li}^+ (cm^2s^{-1})	A	B	C	A	B	C
	5.69×10^{-15}	3.01×10^{-14}	1.60×10^{-15}	1.16×10^{-14}	2.33×10^{-14}	1.08×10^{-15}
$TiNb_6O_{17}$	Anodic peak			Cathodic peak		
D_{Li}^+ (cm^2s^{-1})	A	B	C	A	B	C
	1.12×10^{-13}	3.72×10^{-13}	6.13×10^{-14}	5.35×10^{-14}	3.43×10^{-13}	1.56×10^{-14}

Table 1. Calculated D_{Li}^+ values of (a) $TiNb_2O_7$ and (b) $TiNb_6O_{17}$ anodes from the CV results.

SOD), because the measurement is run by applying a low amplitude signal around an equilibrium state[26–29]. Figure 9(a) shows the Nyquist plot of $TiNb_2O_7$ and $TiNb_6O_{17}$ at the open circuit voltage (OCV) and an equivalent circuit (insert image). Each Nyquist plot was composed of a high-frequency semicircle and Warburg tail region followed by a steep sloping line in the low-frequency region[27]. The R_1 and C_{dl} are the ohmic resistance between the electrolyte and surface of the electrode and double layer capacitance. The high-frequency semicircle means the charge-transfer resistance (R_{ct}) relevant to the interfacial Li-ion transfer. The Z_w is the Warburg impedance, which is related to Li-ion diffusion to the structure of the active materials and corresponds to the tail at a low frequency. Compared to R_{ct}, the $TiNb_6O_{17}$ anode shows a smaller R_{ct} (58Ω) than that of the $TiNb_2O_7$cell (85 Ω). This means that the $TiNb_6O_{17}$ anode has a faster Li insertion process in the surface area than $TiNb_2O_7$. Figure 9(b) presents a plot of the real part resistance with the inverse square root of the angular speed in the low-frequency range of $TiNb_2O_7$ and $TiNb_6O_{17}$ anodes at the OCV state. The Warburg factor (σ) is determined from the slope, and is substituted using equation (Eq. 2 and 3):

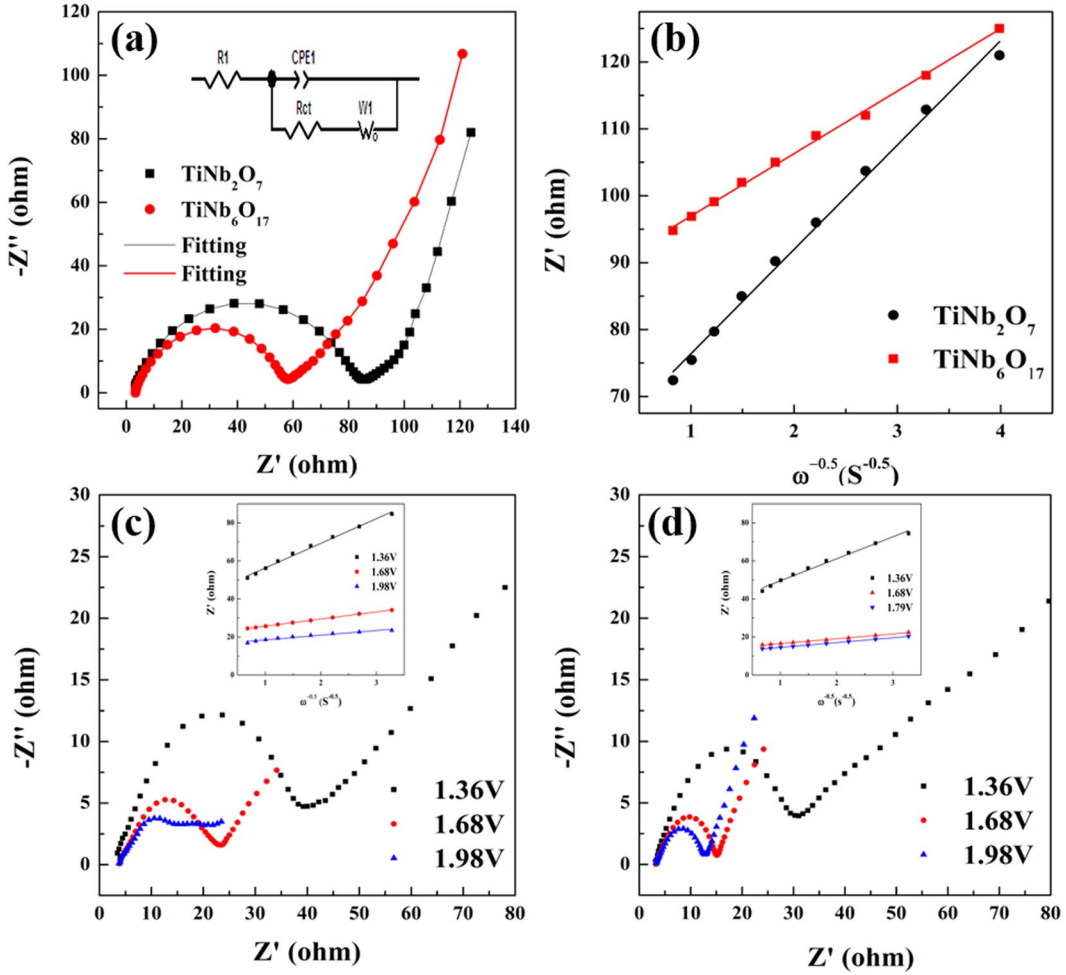

Figure 9. (**a**) Nyquist plots of $TiNb_2O_7$ and $TiNb_6O_{17}$ anodes at OCV state, (**b**) relationship between imaginary resistance (Z') and inverse square root of angular speed (at $\omega^{-0.5}$) low frequency region, (**c**) Nyquist plots of $TiNb_2O_7$ and (**d**) $TiNb_6O_{17}$ (Inert images: relationship between Z' and $\omega^{-0.5}$).

	D_{Li}^+ (cm^2s^{-1}) (OCV)	D_{Li}^+ (cm^2s^{-1}) (1.36 V)	D_{Li}^+ (cm^2s^{-1}) (1.68 V)	D_{Li}^+ (cm^2s^{-1}) (1.98 V)
$TiNb_2O_7$	4.57×10^{-14}	6.64×10^{-14}	7.91×10^{-13}	1.85×10^{-12}
$TiNb_6O_{17}$	1.27×10^{-13}	2.94×10^{-13}	1.12×10^{-11}	4.57×10^{-11}

Table 2. Calculated D_{LI}^+ values of (a) $TiNb_2O_7$ and (b) $TiNb_6O_{17}$ anodes from the EIS results.

$$Z' = R_1 + R_{ct} + \sigma\omega^{(-1/2)} \tag{2}$$

$$D_{Li} = \frac{R^2T^2}{2A^2n^2F^4C^2\sigma^2} \tag{3}$$

where Z' is the real part resistance; ω is the angular frequency; R is the gas constant; T is the absolute temperature; A is the surface area of the electrode; F is the Faraday constant; and C is the molar concentration of Li ion in an active material. Equations (2) and (3) were used to calculate the Warburg factor and lithium diffusion coefficient, respectively. Table 2 lists the calculated D_{Li^+} from the obtained σ. The D_{Li^+} value of $TiNb_2O_7$ and $TiNb_6O_{17}$ anodes at the OCV state was 4.57×10^{-14} cm^2s^{-1} and 1.27×10^{-13} cm^2s^{-1}, respectively. As a result, the $TiNb_6O_{17}$ anode has a better lithium diffusion process than the $TiNb_2O_7$ anode. Although it is not the charge/discharge state, the results revealed the improved lithium diffusion kinetics of $TiNb_6O_{17}$ at the equilibrium state because the more open Li ion insertion site of $TiNb_6O_{17}$ than that of $TiNb_2O_7$ affects the barrier energy and electrostatic interaction regarding the Li^+ insertion mechanism.

To investigate the Li-ion diffusion properties of two TNO materials at the charge state, *ex-situ* EIS experiments were performed on $TiNb_2O_7$ and $TiNb_6O_{17}$ anodes at three oxidation reaction potentials of $Nb^{3+} \rightarrow Nb^{4+}$(1.36 V),

$Nb^{4+} \rightarrow Nb^{5+}$(1.68 V), and $Ti^{3+} \rightarrow Ti^{4+}$(1.98 V) in Fig. 6 (c),(d). Before the EIS experiments, the discharge and charge were processed during 1 cycle and the discharge was then conducted to the cut off potential of 1.0 V. Figure 9(c) $TiNb_2O_7$ and (d) $TiNb_6O_{17}$ present Nyquist plots of the two anodes from EIS (Inert images: plot of the real part resistance with the inverse square root of angular speed in the low-frequency range at three oxidation potential). The calculated D_{Li^+} value is listed in Table 2 with a value at the OCV state. Compared to D_{Li^+} of two TNO anodes from EIS, $TiNb_6O_{17}$ showed higher D_{Li^+} values of 2.94×10^{-13} cm^2s^{-1}, 1.12×10^{-11} cm^2s^{-1}, and 1.85×10^{-12} cm^2s^{-1} at 1.36 V, 1.68 V, and 1.98 V, respectively, than those of $TiNb_2O_7$ (6.64×10^{-14} cm^2s^{-1}, 1.12×10^{-11} cm^2s^{-1}, and $4.57 \times 10^{-11}cm^2s^{-1}$). The D_{Li^+} values of $TiNb_6O_{17}$ were 4.4 times (1.36 V), 14 times (1.68 V), and 25 times (1.98 V) higher than those of $TiNb_2O_7$. Compared to the SSCV results, the D_{Li^+} values of $TiNb_6O_{17}$ showed different multiples except for the value at 1.68 V (20, 12, and 38 times at A_{p1}-1.36 V, A_{p2}-1.68 V, and A_{p3}-1.98 V, respectively, from SSCV) but exhibited similar tendency showing higher D_{Li^+} at all redox potentials than $TiNb_2O_7$. In particular, the gap of D_{Li^+} at 1.68 V (A_{p2} peak at CV) meaning that the two phase regions coincide well with the results of SSCV (14 and 12 fold, respectively.) Therefore, $TiNb_6O_{17}$ has better lithium diffusion properties than $TiNb_2O_7$ due to its structure inducing a larger open lithium site and a number of Li-ion transport paths during the charge processes.

GITT was conducted to determine the Li^+ chemical diffusion coefficient and analyze the phase transition of the two TNO materials. The techniques developed by Weppner and Huggins assumed one-dimensional diffusion in a solid solution electrode and a uniform current distribution throughout the electrode and estimated the electrochemically active area from the structure of the active material particles not for the diffusion reaction between the electrode surface and electrolyte[31–37]. At the transitional GITT, a small constant current was applied to an electrode during a short time and the electrode was left to stand after reaching the OCV state[31–35]. In this study, GITT was performed on the TNO materials to determine the D_{Li^+} at a single phase and two phase region as a function of the voltage for the cut off range of the charge/discharge cycle, 1.0–3.0 V. Figure 10 shows the GITT curves of (a) $TiNb_2O_7$ and (b) $TiNb_6O_{17}$ during the second cycle. The cells were first discharged at a constant current (0.1 C) for a duration time of 15 min and a rest time of 30 min. The curves showed a similar shape and exhibited three plateau regions meaning the solid-solution regions ($Ti^{4+} \leftrightarrow Ti^{5+}$ and $Nb^{3+} \leftrightarrow Nb^{4+}$) and two-phase reaction ($Nb^{4+} \leftrightarrow Nb^{5+}$) with the charge-discharge curves. These regions also showed the cyclic voltammetry peaks of C_{p1} ($Ti^{4+} \rightarrow Ti^{3+}$), C_{p2} ($Nb^{5+} \rightarrow Nb^{4+}$), and C_{p3} ($Nb^{4+} \rightarrow Nb^{3+}$); A_{p1}, A_{p2}, and A_{p3} mean the oxidation reaction of $Nb^{3+} \rightarrow Nb^{4+}$, $Nb^{4+} \rightarrow Nb^{5+}$, and $Ti^{3+} \rightarrow Ti^{4+}$in Fig. 6(c),(d), Fig. 10 (c) $TiNb_2O_7$ and (d) $TiNb_6O_{17}$ present the single steps of GITT. The steps are the results measured at the 3th step during the charge state for the same duration and rest time. In Fig. 10(c) and (d), ΔE_τ and ΔE_s shows the change in the cell voltage during the duration time of 15 min from τ_0 to τ_{0+t} and the variation of the cell voltage during the rest time of 30 min. The voltage changes from the steps are recorded as a function of time and the lithium diffusion coefficient were calculated using the following equation based on Fick's second law[32].

$$D_{Li^+} = \frac{4}{\pi}\left(\frac{m_B V_M}{M_B A}\right)^2 \left(\frac{\Delta E_S}{\tau(dE_\tau/d\sqrt{\tau}}\right)^2 \left(\tau \ll \frac{L^2}{D_{Li^+}}\right) \quad (4)$$

where V_M is the molar volume of the active material; M_B is molecular weight of the materials; m_B is the mass of the active materials in an electrode; L is the lithium diffusion distance (thickness of the electrode); A is the electrode area; and τ is the duration time. When the change in cell voltage with duration time exhibited a linear relationship on plotting against $\tau^{1/2}$, equation (4) can be changed to the following simple equation[32]

$$D_{Li^+} = \frac{4}{\pi\tau}\left(\frac{m_B V_M}{M_B A}\right)^2 \left(\frac{\Delta E_S}{\Delta E_S}\right)^2 \left(\tau \ll \frac{L^2}{D_{Li^+}}\right) \quad (5)$$

This equation assumes that the molar volume (V_M) is stable with the change in Li content in an active material. In this study, the Li^+ diffusion coefficient of the two TNO materials could be calculated, as shown in Fig. 10. (c)–(e). Figure 10.(e) shows the linear relationship between the single steps in Fig. 10. (c),(d). The Li^+ diffusion coefficients of the two TNO materials from the GITT results are presented as a function of SOC (%) vs. Log (D_{Li^+}) during the charge state in Fig. 10. (f). The coefficients were calculated at all steps during the GITT measurements except for the 1st step and the end two steps of the end due to the large voltage variations. The two cells showed three minimum Li^+ diffusion coefficient points in Fig. 10.(f) and the voltages representing the points are shown. These minimum diffusion coefficients suggest a phase transition for strong attractive interactions between the intercalation species and the host matrix or some order-disorder transition during cycling[24,32]. Compared to the SSCV and EIS results, the voltages are the three redox potentials of TNO materials, in which the cell voltages of $TiNb_2O_7$ and $TiNb_6O_{17}$ are 1.42 V~1.38 V ($Nb^{3+} \rightarrow Nb^{4+}$), 1.71~1.75 V ($Nb^{4+} \rightarrow Nb^{5+}$), and 2.01~2.03 V ($Ti^{3+} \rightarrow Ti^{4+}$) vs. 1.36 V, 1.68 V, and 1.98 V, respectively, from the SSCV and EIS measurements. This explains why the plot from GITT has an electrochemical reaction mechanism of two TNO materials with SSCV and EIS. The Li^+ diffusion coefficients of $TiNb_2O_7$ and $TiNb_6O_{17}$ from three points were calculated to be 1.11×10^{-11} and 6.70×10^{-11} cm^2s^{-1} ($Nb^{3+} \rightarrow Nb^{4+}$), 2.74×10^{-11} and 2.23×10^{-10} cm^2s^{-1} ($Nb^{4+} \rightarrow Nb^{5+}$), and 1.03×10^{-10} and 7.47×10^{-10} cm^2s^{-1} ($Ti^{3+} \rightarrow Ti^{4+}$). The coefficients of $TiNb_6O_{17}$ showed higher values than that of $TiNb_2O_7$ at all positions with the other Li^+ diffusion measurements, which indicates that $TiNb_6O_{17}$ has superior Li^+ diffusion kinetics than $TiNb_2O_7$ owing to its larger unit cell volume. Compared to the diffusion coefficients of each transition region, the values increased from the ($Nb^{3+} \rightarrow Nb^{4+}$) reaction to the ($Ti^{3+} \rightarrow Ti^{4+}$) reaction, which correspond to the EIS results in Table 2. Among the three diffusion values, the diffusion coefficients of the ($Nb^{4+} \rightarrow Nb^{5+}$) reaction showed the largest increase from $TiNb_2O_7$ to $TiNb_6O_{17}$ and also corresponds to the EIS

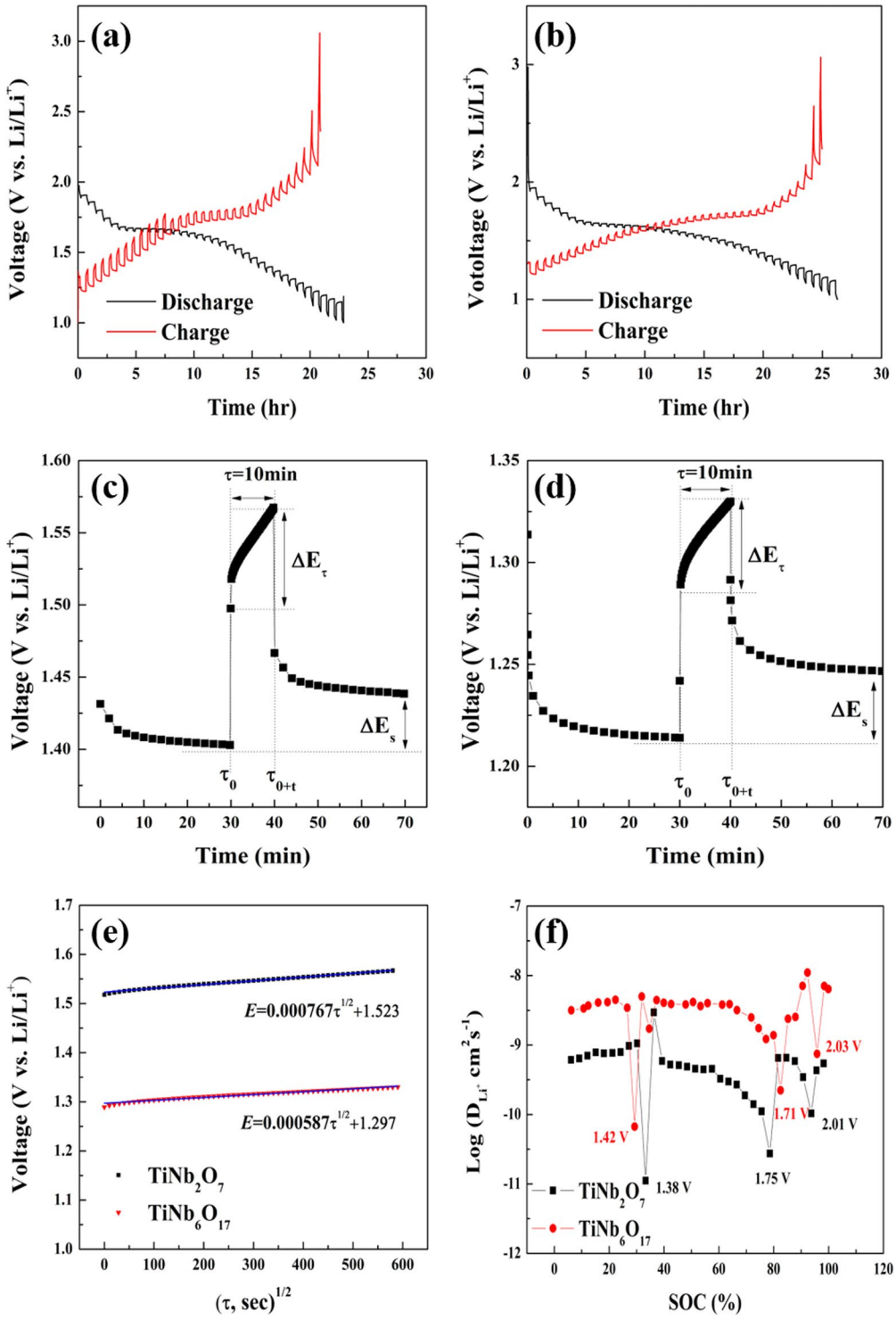

Figure 10. Charge/discharge GITT curves of (**a**) $TiNb_2O_7$ and (**b**) $TiNb_6O_{17}$, single step of the relationship of single steps for (**c**) and (**d**) (V vs. $\tau^{1/2}$), (**e**) and (**f**) lithium diffusion coefficients calculated from GITT for $TiNb_2O_7$ and $TiNb_6O_{17}$ as a function of the SOC at the charge process.

results. These trends suggest that the oxidation reaction is a two phase transition region of TNO materials with the charge-discharge curves and cyclic voltammetry results (the most reaction region). In the event of SSCV, the measurements showed a different tendency with EIS and GITT. The coefficients of the ($Nb^{4+} \rightarrow Nb^{5+}$) reaction ($A_{p2}$) showed the largest values and the diffusion coefficients of the ($Nb^{3+} \rightarrow Nb^{4+}$) reaction showed the largest increase from $TiNb_2O_7$ to $TiNb_6O_{17}$. This may be due to the inaccuracy of the SSCV measurements in this study. Compared to A_{p2}, both A_{p1} and A_{p3} showed a small peak current and a broad shape. Therefore, the diffusion coefficients of the two peaks may be not precise values.

Conclusions

Galvanostatic charge-discharge, cyclic voltammetry, and rate capability test were conducted to analyze the electrochemical performance and properties of $TiNb_6O_{17}$ and $TiNb_2O_7$. From the results, two TNO materials showed three similar plateau regions and three redox peaks corresponding to two Nb redox and one Ti redox reaction. $TiNb_6O_{17}$ showed higher capacities of 284mAh/g than that of $TiNb_2O_7$ 264mAh/g. In the rate capability test, $TiNb_6O_{17}$ exhibited improved rate capacity of 80mAh/g at 30 C than 19mAh/g for $TiNb_2O_7$. SSCV, EIS, and GITT measurement were taken to investigate the performance and lithium diffusion properties related to the unit cell volume of the two TNO materials. The anodic and cathodic Li^+ diffusion coefficients from SSCV were in the range of 10^{-14} to 10^{-15} cm^2s^{-1} for $TiNb_2O_7$ and 10^{-13} to 10^{-14} cm^2s^{-1} for $TiNb_6O_{17}$. The anodic diffusion coefficients of $TiNb_6O_{17}$ were 5 times ($Nb^{3+} \rightarrow Nb^{4+}$), 15 times ($Nb^{4+} \rightarrow Nb^{5+}$), and 14 times ($Ti^{3+} \rightarrow Ti^{4+}$). From the EIS measurement, the coefficients were in the range of 10^{-12} to $10^{-14}cm^2s^{-1}$ of $TiNb_2O_7$ and 10^{-11} to $10^{-13}cm^2s^{-1}$ of $TiNb_6O_{17}$ at the OCV state and three oxidation potential region of the two TNO materials during the charging process. The three minimum diffusion coefficients points were determined from the GITT measurement. The diffusion coefficients of the two phase transition region ($Nb^{4+} \rightarrow Nb^{5+}$) were improved 10 fold compared to that of $TiNb_2O_7$. CV, EIS, and GITT indicated that $TiNb_6O_{17}$ has better lithium diffusion kinetics and electrochemical performance than $TiNb_2O_7$ because of its large unit cell volume and more open Li^+ insertion site.

References

1. Jo, C. *et al*. Block copolymer directed ordered mesostructured $TiNb_2O$ multimetallic oxide constructed of nanocrystals as high power Li-ion battery anodes. *Chemistry of Materials* **26**, 3508–3514 (2014).
2. Park, H., Song, T. & Paik, U. Porous $TiNb_2O_7$ nanofibers decorated with conductive $Ti_{1-x}Nb_xN$ bumps as a high power anode material for Li-ion batteries. *Journal of Materials Chemistry A* **3**, 8590–8596 (2015).
3. Lou, S. *et al*. Facile synthesis of nanostructured $TiNb_2O_7$ anode materials with superior performance for high-rate lithium ion batteries. *Chemical Communications* **51**, 17293–17296 (2015).
4. Wang, H. *et al*. One-step electrolytic preparation of Si–Fe alloys as anodes for lithium ion batteries. *Functional Materials Letters* **9**, 1650050 (2016).
5. Cheng, Q. *et al*. Bulk $Ti_2Nb_{10}O_{29}$ as long-life and high-power Li-ion battery anodes. *Journal of Materials Chemistry A* **2**, 17258–17262 (2014).
6. Tang, K., Mu, X., van Aken, P. A., Yu, Y. & Maier, J. "Nano-Pearl-String" $TiNb_2O_7$ as Anodes for Rechargeable Lithium Batteries. *Advanced Energy Materials* **3**, 49–53 (2013).
7. Wu, X. *et al*. Investigation on $Ti_2Nb_{10}O_{29}$ anode material for lithium-ion batteries. *Electrochemistry Communications* **25**, 39–42 (2012).
8. Lin, C. *et al*. $Ru_{0.01}Ti_{0.99}Nb_2O_7$ as an intercalation-type anode material with a large capacity and high rate performance for lithium-ion batteries. *Journal of Materials Chemistry A*, **3**(16), 8627–8635. (2015).
9. Jayaraman, S. *et al*. Exceptional performance of $TiNb_2O_7$ anode in all one-dimensional architecture by electrospinning. *ACS applied materials & interfaces* **6**, 8660–8666 (2014).
10. Han, J.-T., Huang, Y.-H. & Goodenough, J. B. New anode framework for rechargeable lithium batteries. *Chemistry of Materials* **23**, 2027–2029 (2011).
11. Takashima, T., Tojo, T., Inada, R. & Sakurai, Y. Characterization of mixed titanium–niobium oxide $Ti_2Nb_{10}O_{29}$ annealed in vacuum as anode material for lithium-ion battery. *Journal of Power Sources* **276**, 113–119 (2015).
12. Lin, C., Wang, G., Lin, S., Li, J. & Lu, L. $TiNb_6O_{17}$: a new electrode material for lithium-ion batteries. *Chemical Communications* **51**, 8970–8973 (2015).
13. Cava, R., Murphy, D. & Zahurak, S. Lithium Insertion in Wadsley-Roth Phases Based on Niobium Oxide. *Journal of the Electrochemical Society* **130**, 2345–2351 (1983).
14. Colin, J.-F., Pralong, V., Hervieu, M., Caignaert, V. & Raveau, B. Lithium insertion in an oriented nanoporous oxide with a tunnel structure: $Ti_2Nb_2O_9$. *Chemistry of Materials* **20**, 1534–1540 (2008).
15. Wang, W. L. *et al*. Solid-state synthesis of $Ti_2Nb_{10}O_{29}$/reduced graphene oxide composites with enhanced lithium storage capability. *Journal of Power Sources* **300**, 272–278 (2015).
16. Tang, S., Lai, M. & Lu, L. Li-ion diffusion in highly (003) oriented $LiCoO_2$ thin film cathode prepared by pulsed laser deposition. *Journal of Alloys and Compounds* **449**, 300–303 (2008).
17. Wen, C. J., Boukamp, B., Huggins, R. & Weppner, W. Thermodynamic and mass transport properties of "LiAl". *Journal of The Electrochemical Society* **126**, 2258–2266 (1979).
18. Park, Y.-U., Shakoor, R., Park, K.-Y. & Kang, K.-S. Charge/Discharge Mechanism of Multicomponent Olivine Cathode for Lithium Rechargeable Batteries. *Journal of Electrochemical Science and Technology* **2**, 14–19 (2011).
19. Meethong, N., Kao, Y.-H., Carter, W. C. & Chiang, Y.-M. Comparative study of lithium transport kinetics in olivine cathodes for Li-ion batteries. *Chemistry of Materials* **22**, 1088–1097 (2009).
20. Yoo, S. & Kang, B. Influence of phase transformation pathways on electrochemical properties by using thermally derived solid-solution LiFePO 4 nanoparticles. *Journal of Materials Chemistry A* **3**, 13906–13912 (2015).
21. Abraham, D. P., Kawauchi, S. & Dees, D. Modeling the impedance versus voltage characteristics of $LiNi_{0.8}Co_{0.15}Al_{0.05}O_2$. *Electrochimica Acta* **53**, 2121–2129 (2008).
22. Hjelm, A.-K. & Lindbergh, G. Experimental and theoretical analysis of LiMn 2 O 4 cathodes for use in rechargeable lithium batteries by electrochemical impedance spectroscopy (EIS). *Electrochimica Acta* **47**, 1747–1759 (2002).
23. Park, C.-K., Park, S.-B., Oh, S.-H., Jang, H. & Cho, W.-I. Li Ion Diffusivity and Improved Electrochemical Performances of the Carbon Coated LiFePO 4. *Bulletin of the Korean Chemical Society* **32**, 836–840 (2011).
24. Hu, L. *et al*. $TiNb_2O_7$ nanorods as a novel anode material for secondary lithium-ion batteries. *Functional Materials Letters* **9**, 1642004 (2016).
25. Bisquert, J., Garcia-Belmonte, G., Bueno, P., Longo, E. & Bulhoes, L. Impedance of constant phase element (CPE)-blocked diffusion in film electrodes. *Journal of Electroanalytical Chemistry* **452**, 229–234 (1998).
26. Piao, T., Park, S. M., Doh, C. H. & Moon, S. I. Intercalation of lithium ions into graphite electrodes studied by AC impedance measurements. *Journal of The Electrochemical Society* **146**, 2794–2798 (1999).
27. Churikov, A. *et al*. Determination of lithium diffusion coefficient in $LiFePO_4$ electrode by galvanostatic and potentiostatic intermittent titration techniques. *Electrochimica Acta* **55**, 2939–2950 (2010).
28. Heubner, C., Schneider, M. & Michaelis, A. Investigation of charge transfer kinetics of Li-Intercalation in $LiFePO_4$. *Journal of Power Sources* **288**, 115–120 (2015).
29. Xie, J. *et al*. Li-ion diffusion kinetics in $LiFePO_4$ thin film prepared by radio frequency magnetron sputtering. *Electrochimica Acta* **54**, 4631–4637 (2009).

30. Mahesh, K., Manjunatha, H., Venkatesha, T. & Suresh, G. Study of lithium ion intercalation/de-intercalation into $LiNi_{1/3}Mn_{1/3}Co_{1/3}O_2$ in aqueous solution using electrochemical impedance spectroscopy. *Journal of Solid State Electrochemistry* **16**, 3011–3025 (2012).
31. Dees, D. W., Kawauchi, S., Abraham, D. P. & Prakash, J. Analysis of the Galvanostatic Intermittent Titration Technique (GITT) as applied to a lithium-ion porous electrode. *Journal of Power Sources* **189**, 263–268 (2009).
32. Rui, X., Ding, N., Liu, J., Li, C. & Chen, C. Analysis of the chemical diffusion coefficient of lithium ions in $Li_3V_2(PO_4)_3$ cathode material. *Electrochimica Acta* **55**, 2384–2390 (2010).
33. Zhu, Y. & Wang, C. Galvanostatic intermittent titration technique for phase-transformation electrodes. *The Journal of Physical Chemistry C* **114**, 2830–2841 (2010).
34. Levi, M. D. & Aurbach, D. Potentiostatic and Galvanostatic Intermittent TitrationTechniques. Characterization of Materials (2012).
35. Tang, K., Yu, X., Sun, J., Li, H. & Huang, X. Kinetic analysis on $LiFePO_4$ thin films by CV, GITT, and EIS. *Electrochimica Acta* **56**, 4869–4875 (2011).
36. Levi, M., Aurbach, D. & Vorotyntsev, M. Interpretation of potential intermittence titration technique experiments for various Li-intercalation electrodes∗. *Condensed Matter Physics* (2002).
37. Lee, J.-G., Kim, B., Cho, J., Kim, Y.-W. & Park, B. Effect of $AlPO_4$-nanoparticle coating concentration on high-cutoff-voltage electrochemical performances in $LiCoO_2$. *Journal of the electrochemical society* **151**, A801–A805 (2004).

Acknowledgements

This study was supported by the Priority Research Centers Program through the National Research Foundation of Korea (NRF), funded by the Ministry of Education, Science and Technology (MEST) of the Korean government (2009–0093818).

Author Contributions

Kwang-Sun Ryu decided the concept of the experiments, discussed the results and reviewed the manuscript. Yong-Seok Lee performed all experiments, analyzed the data and wrote the manuscript.

Additional Information

Competing Interests: The authors declare that they have no competing interests.

Publisher's note: Springer Nature remains neutral with regard to jurisdictional claims in published maps and institutional affiliations.